LA-6827-MS
Informal Report

UC-21

Issued: June 1977

C.3

One-Dimensional Computer Simulations of the Implosion of Simple-Shell Targets with the Los Alamos Two-Beam CO_2 Laser

(Series I)

Charles W. Cranfill

los alamos
scientific laboratory
of the University of California
LOS ALAMOS, NEW MEXICO 87545

An Affirmative Action/Equal Opportunity Employer

UNITED STATES
ENERGY RESEARCH AND DEVELOPMENT ADMINISTRATION
CONTRACT W-7405-ENG. 36

This work was supported by the US Energy Research and Development Administration, Division of Laser Fusion.

Printed in the United States of America. Available from
National Technical Information Service
U.S. Department of Commerce
5285 Port Royal Road
Springfield, VA 22161
Price: Printed Copy $3.50 Microfiche $3.00

ONE-DIMENSIONAL COMPUTER SIMULATIONS OF THE IMPLOSION OF SIMPLE-SHELL TARGETS WITH THE LOS ALAMOS TWO-BEAM CO_2 LASER (SERIES I)

by

Charles W. Cranfill

ABSTRACT

This report summarizes the results of a series of one-dimensional computer simulations of the implosion of spherical targets with the Los Alamos two-beam CO_2 laser. The simulations were done with a Los Alamos version of the laser-fusion code LASNEX originally developed at the Lawrence Livermore Laboratory. The targets studied were simple glass microshells filled with DT gas, and the predicted scaling of neutron and X-ray emissions with variations in target and laser parameters was determined for comparison with experiments currently underway at Los Alamos.

I. INTRODUCTION

With the implementation of the Los Alamos two-beam CO_2 laser as a target-implosion machine, a need has arisen for computer simulations with which to compare near-term target experiments. This report summarizes a series of such simulations done with the Lagrangian laser-fusion code LASNEX originally developed at Lawrence Livermore Laboratory.* Much work on target simulation at the 1.06-μm wavelength of Nd-glass lasers has been reported previously,[1-8] but this appears to be the first detailed study at the 10.6-μm wavelength of CO_2 lasers.

There were two main purposes for this study: first, to aid in the design and interpretation of experiments on the Los Alamos two-beam CO_2 laser; and second, to confirm or improve the accuracy of the physical model used in LASNEX. Accordingly, a simple, easily diagnosed target consisting of a glass microsphere filled with DT gas was chosen. Since such a target was expected to operate in the so-called "exploding pusher" mode, symmetry was not considered to be a problem and only one-dimensional simulations were performed for this study.

In the simulations, the targets were taken to be perfect spherical shells of fused quartz (SiO_2 at density 2.204 gm/cm^3) filled with equimolar mixtures of deuterium (D_2) and tritium (T_2). This ignored inhomogeneities in shell thickness and impurities in glass composition typically present in actual targets, but the resulting errors in predicted target performance should not be severe.

The Los Alamos two-beam CO_2 laser has a temporal pulse shape consisting of a roughly linear rise to peak power followed by an exponential fall. Since target performance is not very sensitive to the shape of the fall, it was decided to use a simple triangular temporal pulse in the simulations (see Figure I.1):

$$\begin{matrix} & \text{(rise)} & & \text{(fall)} \\ P(t)/P_L = t/\alpha T_L & \text{or} & (T_L-t)/(1-\alpha)T_L & , \end{matrix} \quad \text{(I.1a)}$$

$$E(t)/E_L = t^2/\alpha T_L^2 \text{ or } 1-(T_L-t)^2/(1-\alpha)T_L^2. \quad \text{(I.1b)}$$

Here P_L is the peak laser power, E_L is the total laser energy, $T_L \equiv 2E_L/P_L$ is the effective pulse-

*The physical model used in the current Los Alamos version of the code is outlined in the Appendix.

duration, and αT_L is the rise time to peak power. Rough account of the spatial distribution of the laser intensity was taken by reducing the values of P_L and E_L incident on a target of radius R by a Gaussian factor with characteristic width σ (see Figure I.2):

$$P_L'(R)/P_L = E_L'(R)/E_L = 1 - \exp(-2R^2/\sigma^2) \quad . \quad (I,2)$$

Most of the simulations done for this study used one of the following sets of laser parameters:

$$P_L=.6TW,\ E_L=.72kJ,\ T_L=2.4ns,\ \sigma=100\mu m \ , \quad (I.3a)$$

$$P_L=.5TW,\ E_L=.60kJ,\ T_L=2.4ns,\ \sigma=100\mu m \ . \quad (I.3b)$$

These values were chosen in accordance with the previous performance of the Los Alamos two-beam CO_2 laser on flat targets. When implosion experiments were begun, however, it was found that spherical targets couple with the laser cavity to produce undesirable pre-oscillation which can damage the targets before the main pulse arrives. This necessitated lowering the operating level of the laser to the following values:

$$P_L\cong.4TW,\ E_L\cong.48kJ,\ T_L\cong2.4ns,\ \sigma\cong100\mu m \ . \quad (I.3c)$$

In addition, a saturable absorber (SF_6) was inserted in front of the target chamber reducing the on-target power still further.

Rather than re-run all the simulations with a different laser source, the scaling of performance with incident power was determined for one target. This scaling could then be used to extrapolate the code predictions for comparison with the lower-power experimental data currently available.

The remaining sections of this report summarize the detailed results of the simulations. Section II discusses the predicted neutron yields and scaling, Section III discusses the calculated hard X-ray and electron spectra, and Section IV discusses the calculated soft X-ray emissions from these targets. The available experimental results are given for comparison, but since only a fraction of the implosions on the two-beam CO_2 laser have been simple shells, insufficient data exist at this time for a definitive evaluation of the predictive power of LASNEX.

II. CALCULATED NEUTRON PRODUCTION

The predominant nuclear reaction in a DT gas is $D+T\rightarrow n+\alpha$, so the number of neutrons produced is an accurate indication of the extent of fusion burn achieved in a target. Figures II.1-5 show the calculated neutron yields for various target and laser parameters. Because of uncertainties in the laser characteristics and target physics, the absolute numbers of neutrons predicted are not likely to be very accurate. However, the relative trends shown by the curves should be fairly reliable. As experimental data are accumulated on the two-beam CO_2 laser, the code can be modified to improve its absolute accuracy.

Figure II.1 illustrates the scaling of neutron yield with pulse rise time to peak power. Simulations were done for αT_L=.16,.24,.32,.40ns with the other laser parameters fixed at the values given in (I.3a). Curves are plotted for the two initial target radii R_I=45 and 75 μm, and the respective corrected peak powers were P_L'=.20 and .40TW. Also, the aspect ratio was $R_I/\Delta R$=75, the DT fill pressure was 10 atm, and the absorption fraction was β=.10. The dashed and solid curves distinguish between the two

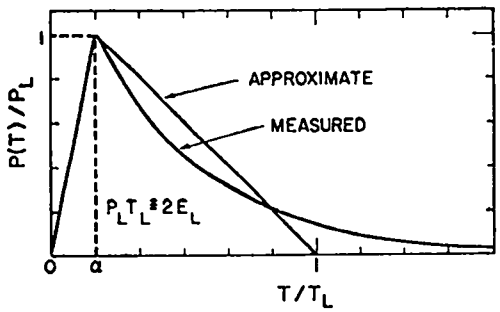

Fig. I.1. Laser temporal pulse shape.

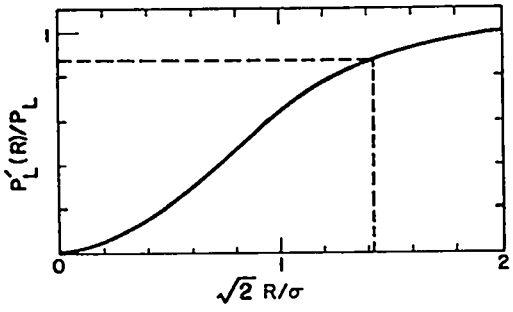

Fig. I.2. Laser spacial pulse shape.

supra-thermal generation temperatures (A.1,2), and it is seen that the results for the second formula with γ=-36 are closely approximated by results for the first formula with γ=3 to 5. All curves show a trend toward increased yield as rise time is decreased. The current best estimate of the rise time of the two-beam CO_2 laser pulse is .20ns.

Figure II.2 illustrates the scaling of neutron yield with initial target radius. Simulations were done for R_I=45,60,75,90,105μm, with the aspect ratio fixed at $R_I/\Delta R$=75. The curves on the left half correspond to the laser parameters (I.3a) with the indicated rise times, where the DT fill pressure was 10 atm, and the absorption fraction β=.10. The curves on the right half correspond to the laser parameters (I.3b) with the indicated fill pressures and absorption fractions, where the rise time was αT_L=.16ns. All these simulations used the laser-power correction (I.2) with σ=100μm and the supra-thermal generation temperature (A.2) with γ=-36. Note that the optimum radius is near R_I=90μm, but the yield varies little between R_I=75 and 105μm.

Figure II.3 illustrates the scaling of neutron yield with initial DT fill pressure. Simulations were done for the pressures 1.0, 3.2, 10, 32, 100 atm. The curves correspond to the laser parameters (I.3b) with the indicated absorption fractions, where the rise time was αT_L=.16ns, the initial radius was R_I=75μm, and the aspect ratio was $R_I/\Delta R$=75. The corrected peak laser power was P_L=.333TW, and the supra-thermal generation temperature (A.2) was used with γ=-36. All curves show a trend toward increased yield as the fill pressure is decreased.

The 10% absorption cases were also run with the DT frozen on the inside of the glass shell, and the results are plotted as the dashed curve. Note the curious prediction that solidifying the fuel reduces the yield for initial pressures less than 15 atm. It has not yet been determined if this is a real effect or just an inaccuracy in the simulations. For higher pressures, the predicted yield is substantially increased (e.g., by a factor of 15 at 100 atm.) by solidifying the fuel. However, it appears that with the present lasers, the maximum benefits should be obtained by simply going to lower-pressure gas-filled shells.

Figure II.4 illustrates the scaling of neutron yield with absorption fraction. Simulations were done for β=.05, .10, .20, .40. The initial DT fill pressures were as indicated, and the other parameters were the same as those described for Fig. II.3. The yield scales roughly as $\beta^{3.3}$, so the absorption fraction is an important parameter to

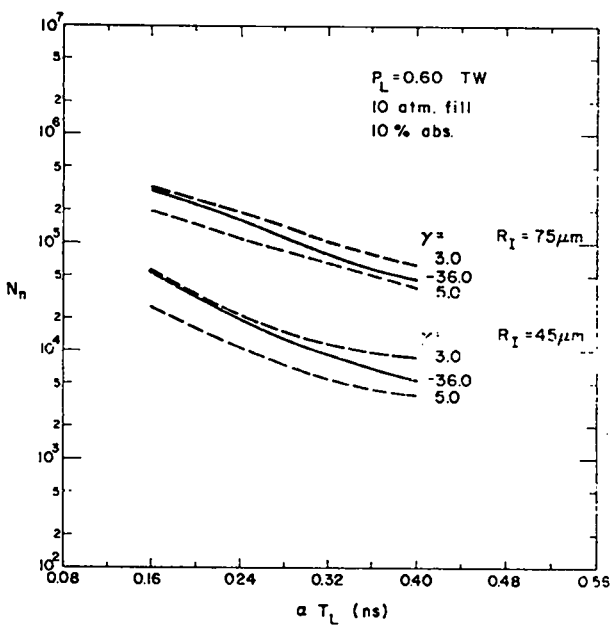

Fig. II.1. Neutrons produced vs. pulse rise time.

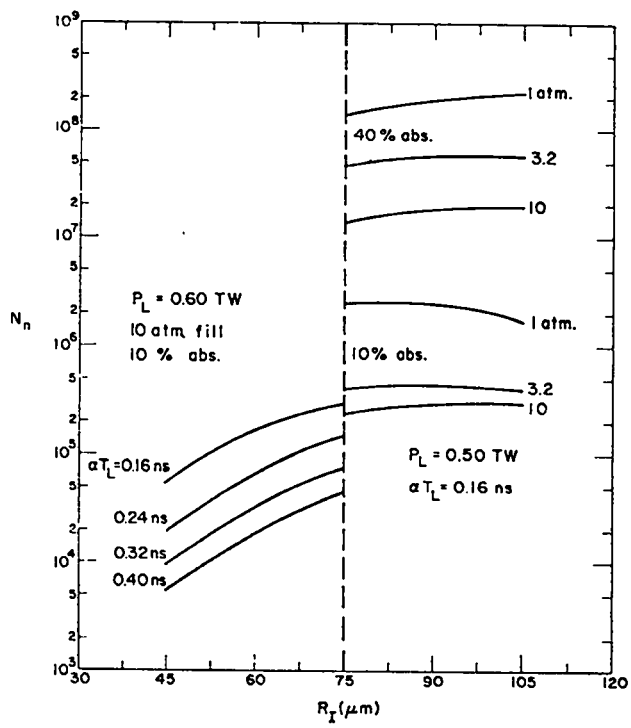

Fig. II.2. Neutrons produced vs. target radius.

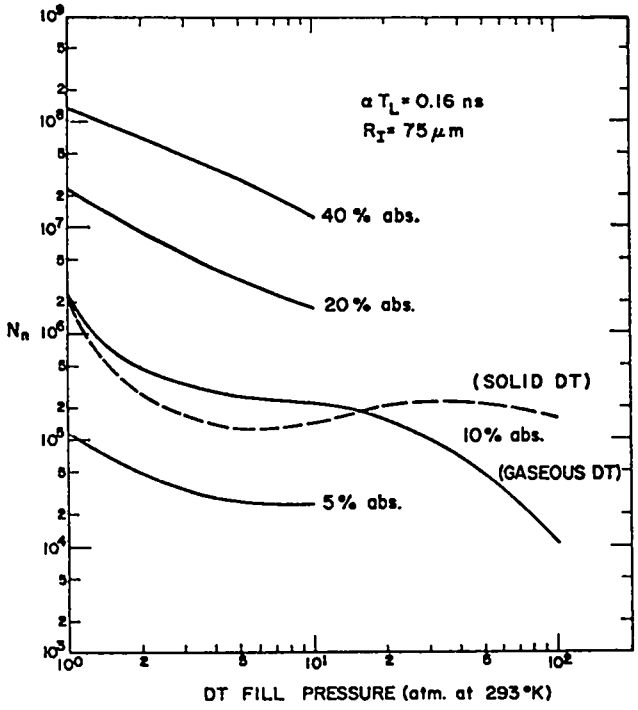

Fig. II.3. Neutrons produced vs. DT fill pressure.

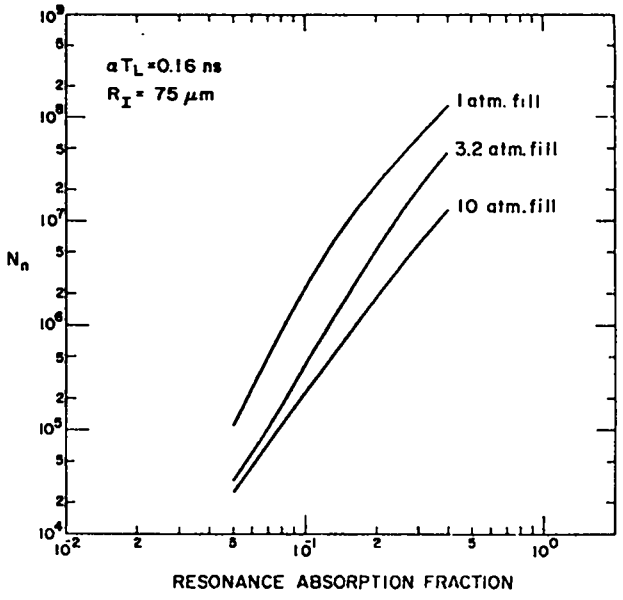

Fig. II.4. Neutrons produced vs. resonance absorption fraction.

determine. Particle-in-cell code simulations in planar geometry give a range $\beta \cong .3$-$.5$ depending on the polarization, incidence angle, and intensity of the laser light.[9] Experiments at Los Alamos have partially confirmed this by measuring $\beta \cong .45$ for CO_2 laser light normally incident on flat targets.[10] These results don't directly apply to spherical targets, however, so further experiments are planned for the near future.

Figure II.5 illustrates the scaling of neutron yield with peak laser power. Simulations were done for $P_L' = .25$, 1.0, 4.0, 16TW, with fixed pulse duration $T_L = 2.4$ns and rise time $\alpha T_L = .24$ns. The initial target radius was $R_I = 75\mu m$, the aspect ratio was $R_I/\Delta R = 75$, the fill pressure was 1 atm, and the absorption fraction was $\beta = .20$. The supra-thermal generation temperature (A.2) was used with $\gamma = -36$, and the correction factor (I.2) relating the above values of P_L' to P_L was 2/3 corresponding to $\sigma \cong 100\mu m$. The yield scales roughly as $(P_L')^{2.8}$ between .25 and 1.0TW, so a factor of 2 change in power causes a factor of ~7 change in yield. This allows the predictions of the target simulations to be compared with experiments done at different power levels.

In January of 1977 a series of target experiments was begun on the Los Alamos two-beam CO_2 laser.

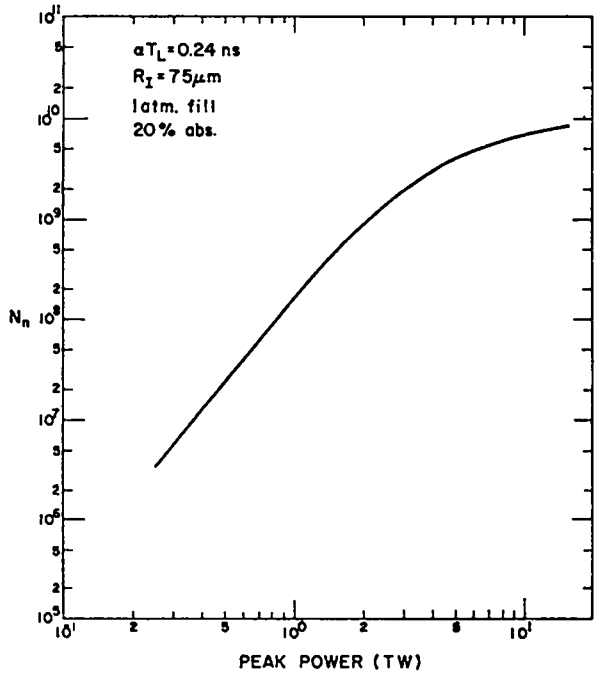

Fig. II.5. Neutrons produced vs. peak laser power.

Although this series is not devoted solely to spherical implosions, more than 50 DT-filled glass shells have been shot. However, many of these contained complex structures not modeled in the one-dimensional simulations, so only 13 good shots are currently available for direct comparison with the LASNEX predictions reported here.

These 13 shots can be divided into two groups whose properties are summarized in Table II.1 along with a LASNEX simulation result. The listed uncertainties are the standard deviations of the data, except that the neutron-yield deviations were divided by the square root of the numbers of shots to give the estimated uncertainties of the group means. The LASNEX simulation yield was obtained from Fig. II.4 by lowering the 10-atm curve by a factor $(.25/.5)^{2.8}$ to correct for the reduced laser power in accordance with Fig. II.5. The value $\beta=.16$ was chosen to fit the experimental neutron yields. Clearly, these data are insufficient to allow a detailed evaluation of the LASNEX simulations, but they do appear to be consistent with the predictions.

TABLE II.1

COMPARISON OF EXPERIMENTAL AND THEORETICAL NEUTRON YIELDS

	# Shots	R_I(μm)	ΔR(μm)	Fill(atm)	P_L(TW)	$N_n(10^5 n)$
Group I	6	75.8±0.8	1.0±0.1	10	.245±.058	1.36±0.44
Group II	7	98.5±1.8	0.8±0.1	10	.240±.054	1.36±0.76
LASNEX	(β=.16)	75.0	1.0	10	.25	1.35

III. CALCULATED HARD X-RAY AND HOT-ELECTRON PRODUCTION

Both theoretical and experimental evidence[8,9] indicate that the interaction of a high-intensity laser with a plasma produces a supra-thermal electron component. In LASNEX such a component is generated at the critical density surface with a Maxwellian energy distribution at a temperature θ_H given by either (A.1) or (A.2). The latter prescription for θ_H is favored at Los Alamos since it includes the explicit dependence on laser intensity I, laser wavelength λ, and background electron temperature θ_C. The exponents in (A.2) were determined from particle-in-cell code simulations in which the predominant laser-plasma interaction was resonance absorption.[9]

The chief experimental diagnostics available for the study of hot electrons are ion, electron, and hard X-ray spectra. The last of these is the simplest to obtain experimentally, so for comparison, the time-integrated hard X-ray spectra were calculated for each LASNEX simulation done for this study.

Figures III.1,2 show examples for a simulation using the laser parameters (I.3b) with a rise time $\alpha T_L=.16$ns. The target radius was $R_I=90$μm, the aspect ratio was $R_I/\Delta R=75$, the fill pressure was 10 atm, and the absorption fraction was $\beta=.10$. The effective peak power (corrected by (I.2) with $\sigma=100$μm) was .4TW corresponding to $I\lambda^2=.44\times10^{17}$ W·μm^2/cm^2. The supra-thermal generation temperature (A.2) was used with $\gamma=-36$. Note that the hard X-ray spectra are well fit by straight lines whose slopes give a temperature which varied from 12keV at .2ns (near peak laser power) to 13keV at 2.4ns (near laser shut-off). The X-ray temperature at 2.4ns remained in the range 14±1keV when the absorption fraction was varied from .05 to .40.

Figures III.3,4 show the instantaneous electron spectra produced at two times in the simulation described above. The straight-line fits give a temperature which varies from 24keV at 0.2ns to 13keV at 2.4ns. Clearly, the peak instantaneous electron temperatures can be considerably hotter than the time-averaged values derived from the integrated hard X-ray spectra.

Figure III.5 shows a composite plot of many experimentally determined hot-electron temperatures reported in the literature by laser groups around the world.[9] Data are included for both 1.06μm and 10.6μm wavelengths and both ion and hard X-ray measurements. Note that when plotted versus the parameter $I\lambda^2$, the data are reasonably consistent with a single curve whose slope varies from $\frac{2}{3}$ at low intensity to $\frac{1}{4}$ at high intensity. The break in the curve occurs just where the laser ponderomotive force becomes large enough to significantly steepen the plasma density profile. The particle-in-cell code simulation point at $I\lambda^2=10^{16}$ W·μm^2/cm^2 is seen to be in good agreement with the experiments.[9] Furthermore, the temperature of ~14keV derived from the time-integrated X-ray spectra calculated by the LASNEX simulations described above is also seen to be in good agreement with the data at the appropriate mean value $I\lambda^2=.22\times10^{17}$ W·μm^2/cm^2. Indeed, this was the motivation for the choice $\gamma=-36$.

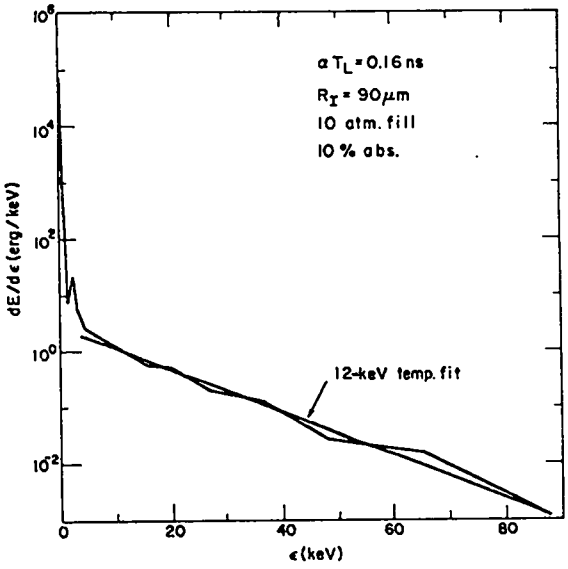

Fig. III.1. X-ray spectrum (time-integrated to 0.2ns).

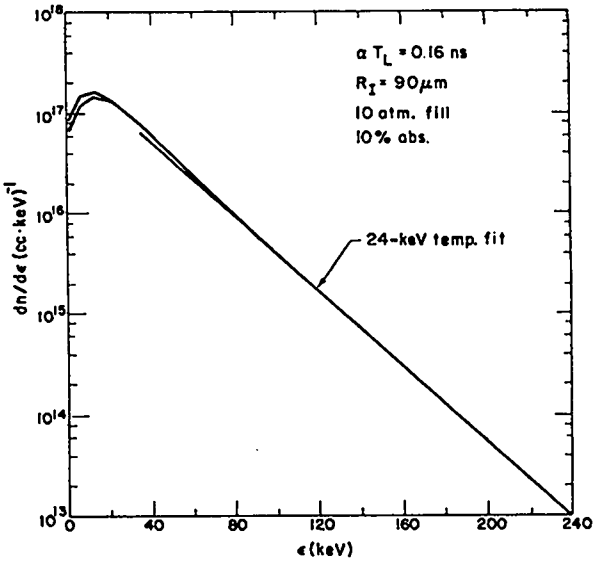

Fig. III.3. Electron spectrum (instantaneous at 0.2ns).

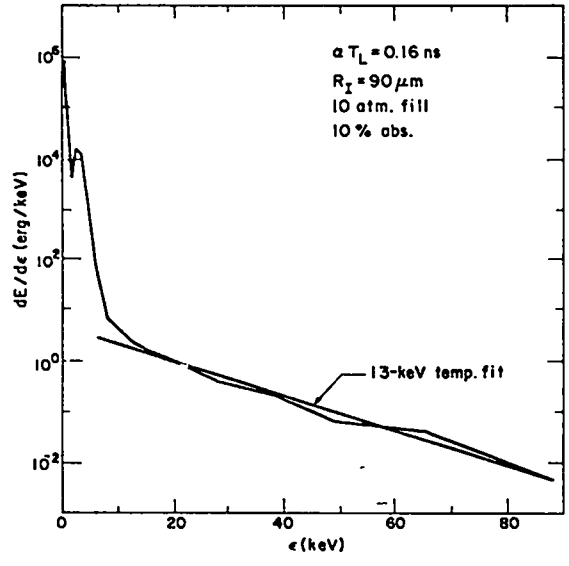

Fig. III.2. X-ray spectrum (time-integrated to 2.4ns).

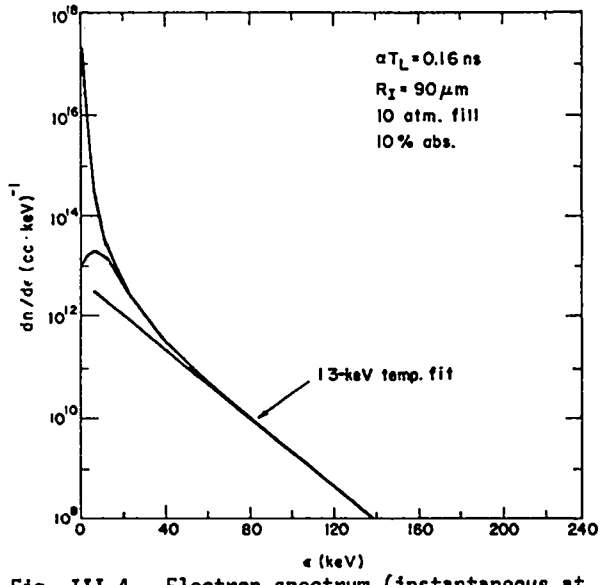

Fig. III.4. Electron spectrum (instantaneous at 2.4ns).

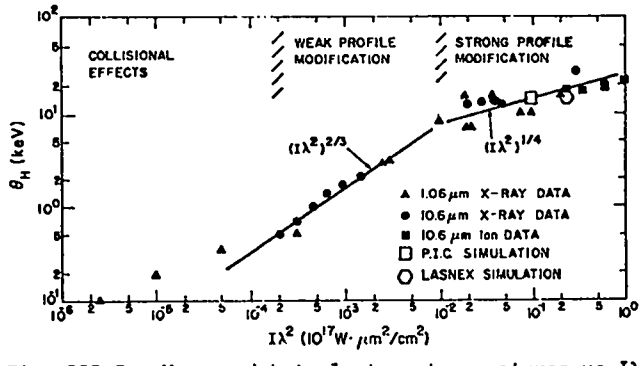

Fig. III.5. Measured hot-electron temperatures vs $I\lambda^2$.

IV. CALCULATED SOFT X-RAY PRODUCTION

The final diagnostic simulated in this study was the soft X-ray emission. Each LASNEX run produced an output file which could be postprocessed by a code TDG (developed by Hank Shay at Lawrence Livermore Laboratory) to generate a soft X-ray spectrum, power time profile, and pinhole picture. This code allows arbitrary filter functions and resolutions to be specified, and the pinhole pictures can be either time-integrated or time-resolved.

For this simulation series, a 12.7μm beryllium filter was chosen, where the corresponding X-ray transmission function is shown in Fig. IV.1. Filtered X-ray spectra, power profiles, and time-integrated pinhole pictures were then generated for each target studied. Figures IV.2-4 show examples for a simulation using the laser parameters (I.3b) with a rise time of .16ns. The target radius was R_I=90μm, the aspect ratio was $R_I/\Delta R$=75, and the fill pressure was 10 atm. The effective peak power (corrected by (I.2) with σ=100μm) was .4TW, and the supra-thermal generation temperature (A.2) was used with γ=-36. Computer runs were done for the four absorption fractions β=.05, .10, .20, .40.

Figures IV.2-4 illustrate three basic trends in the calculated soft X-ray emission as absorption fraction increases:

(i) the continuum free-bound emission (above 2.4 keV) increases relative to the line emission (see Fig. IV.2);

(ii) the early-time peak in the power profile increases relative to the late-time peak (see Fig. IV.3);

(iii) the inner peak in the pinhole picture densitometer trace increases relative to the outer peak (see Fig. IV.4).

These trends should provide useful consistency checks for the absorption fraction as measured by other methods.

Figure IV.5 shows an experimentally obtained pinhole picture densitometer trace for one of the Group I shots summarized in Table II.1. The laser power for this shot was .268TW, and the neutron yield was 1.2×10^5. The trace illustrates three features which are typical of the pinhole pictures of implosions on the Los Alamos two-beam CO_2 laser: (i) a central spot of radius ~10μm; (ii) an inner ring of radius ~20μm; and (iii) an outer ring of radius ~100μm. The second and third features agree qualitatively with the calculated traces shown in Figs. IV.4a,b, although the positions of the rings relative to the initial target radius are somewhat different. However, the small central spot observed experimentally is not reproduced by the LASNEX simulations. This leads one to suspect that some anomalous process, such as fuel-pusher mix or shell breakup, is allowing hot high-Z material to reach the target center. This phenomenon requires further study.

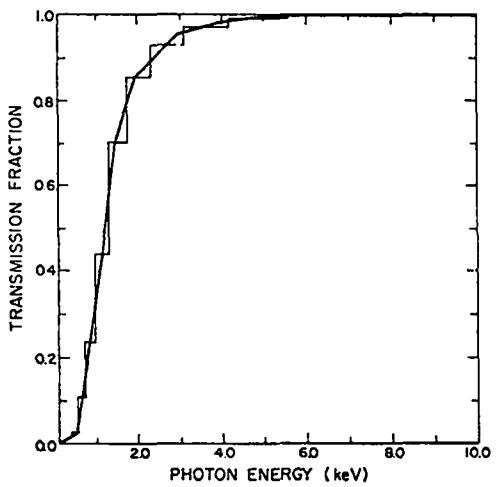

Fig. IV.1. 0.5 mil Be filter transmission function.

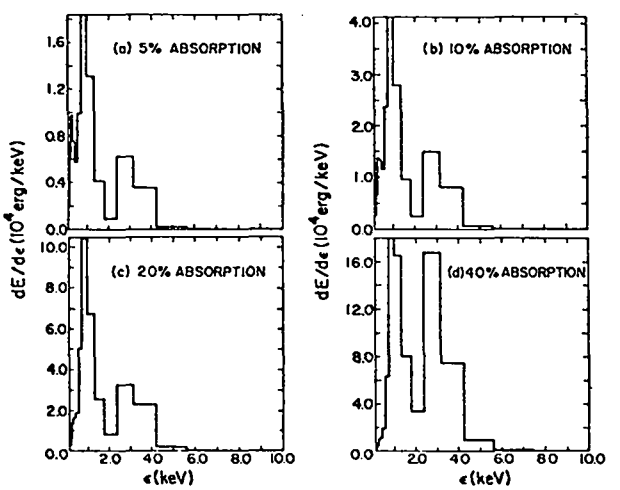

Fig. IV.2. Filtered soft X-ray spectra.

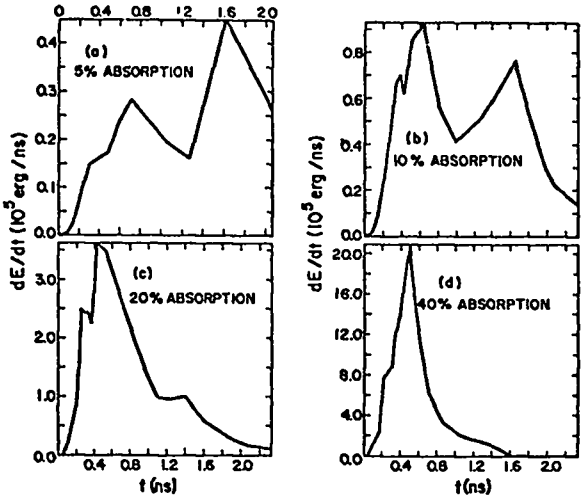

Fig. IV.3. Soft X-ray time profiles.

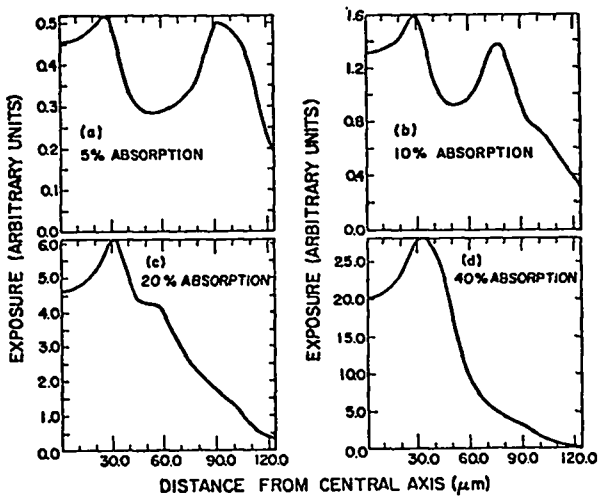

Fig. IV.4. Soft X-ray pinhole pictures (10-μm resolution)

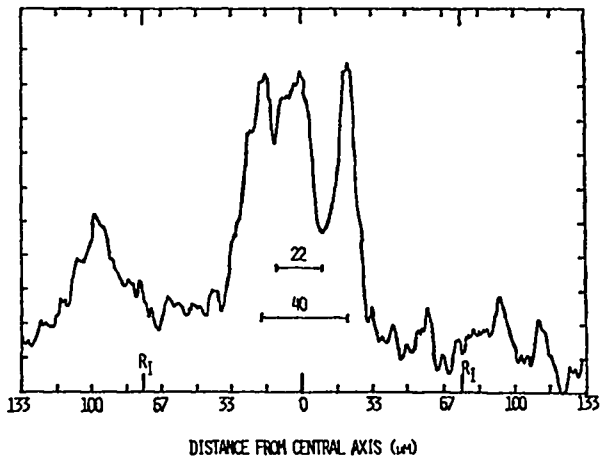

Fig. IV.5. Experimental pinhole picture (10-μm resolution)

ACKNOWLEDGEMENTS

Several people at the Los Alamos Scientific Laboratory aided in the comparison of the simulation results with the available experimental data. The raw neutron data summarized in Table II.1 were recorded and organized by Dan Bannerman and Ping Lee. The hot-electron data in Fig. III.5 were compiled by Damon Giovanielli and Gene McCall, and the supra-thermal electron generation prescription used in most of the simulations was developed by Dave Forslund, Joe Kindel, and Ken Lee. The pinhole-picture densitometer trace shown in Fig. IV.5 was provided by Dave van Hulsteyn.

Useful advice on the workings of LASNEX was generously provided by George Zimmerman and Dave Kershaw of the Lawrence Livermore Laboratory.

APPENDIX A
PHYSICAL MODEL IN LASNEX

LASNEX is a Lagrangian fluid-dynamics code developed at Lawrence Livermore Laboratory to simulate laser-initiated fusion designs.[11] Basically, the code employs a two-temperature one-fluid description of an electron-ion gas heated by an external laser source. Viscous and conductive transport processes for both the electrons and ions are modeled, and in the two-dimensional axi-symmetric mode, the effects of self-generated or external magnetic fields can be included. The code calculates classical transport coefficients with constraints imposed to prevent the free-streaming flux limits from being exceeded. Ideal-gas equations-of-state are used for the ions, while tabulated Thomas-Fermi-Dirac equations-of-state are used for the electrons. The local instantaneous ionization states are determined from an equilibrium Saha equation.

Superimposed on the Lagrangian electron-ion fluid are three non-thermal particle components. The first is composed of burn products generated by thermonuclear fusion. The code calculates rates for all fusion reactions involving deuterium, tritium, and helium. The charged nuclei produced can be deposited locally, allowed to escape, or transported by single- or multi-group flux-limited diffusion.

The second non-thermal component is composed of X-rays generated by free-free, free-bound, and bound-bound electron transitions. Emissivities and opacities are calculated assuming hydrogenic electron states populated in accordance with local thermodynamic equilibrium. The X-rays are transported by multi-group flux-limited diffusion.

The third non-thermal component is composed of electrons generated by anomalous absorption of high-intensity light from the external laser source. These electrons are transported by multi-group flux-limited diffusion subject to collisional and electromagnetic influences of the background electron-ion fluid.

The light from the external laser source is absorbed by inverse-bremsstrahlung until it reaches a critical-density surface at which the local plasma frequency equals the light frequency. At such a surface a fraction $(1-\beta)$ of the light intensity is reflected, and the rest is dumped into the electrons to simulate anomalous absorption (see discussion below). In the Los Alamos version of LASNEX the light intensity is enhanced near a critical surface in accordance with the local plasma dielectric constant, and the ponderomotive force exerted by the light is included in an attempt to model the density-profile steepening observed in particle-in-cell code simulations.[9]

The fraction β of light intensity absorbed anomalously at a critical surface is used to elevate thermal electrons up into the supra-thermal component mentioned previously. The supra-thermal electrons are generated with an isotropic Maxwellian energy distribution whose temperature is determined by either of two prescriptions:

$$\theta_H = \gamma\theta_C \quad , \gamma>0 \tag{A.1}$$

$$\theta_H = -\gamma\theta_C^{1/2}(I\lambda^2)^{1/4} \quad , \gamma<0 \ . \tag{A.2}$$

Here γ is an input constant, θ_H and θ_C are the respective temperatures (keV) of the hot and cold electron components, and I and λ are the respective intensity (10^{17}W/cm^2) and wavelength (μm) of the laser light.

The first prescription (A.1) for the supra-thermal electron generation was developed at Lawrence Livermore Laboratory to model instability absorption,[8,11] and reasonable agreement with experiments is achieved with the choice γ=4. The second prescription (A.2) was developed at Los Alamos Scientific Laboratory to model resonance absorption,[9] and reasonable agreement with experiments (for $I\lambda^2>10^{15}$ W·μm^2/cm^2) is achieved with the choice γ=-36.

REFERENCES

1. F. J. Mayer, R. R. Goforth, R. R. Johnson, T. A. Crispin, "Yield Scaling in Laser-Driven Target Experiments," Bull. Am. Phys. Soc. 20, 1237 (1975).

2. P. M. Campbell, P. Hammerling, R. R. Johnson, J. J. Kubis, F. J. Mayer, D. C. Slater, "Laser Driven Compression and Neutron Generation with Spherical Shell Targets," Presented at the 6th International Conference on Plasma Physics and Controlled Nuclear Fusion Research, Berchtesgarten, Federal Republic of Germany, October 1976.

3. S. Bertke and E. Goldman, "Computational Design of Laser Target Configurations for Compression Experiments," Bull. Am. Phys. Soc. 21 1153 (1976).

4. J. Delettrez, E. Goldman, E. Thorsos, "Theoretical Interpretation of Recent Experimental Results," Bull. Am. Phys. Soc. 21, 1154 (1976).

5. J. T. Larsen, "Computer Simulation of Laser Driven Implosion of DT Filled Glass Microshells," Bull. Am. Phys. Soc. 20, 1267 (1975).

6. J. F. Holzrichter, H. G. Ahlstrom, D. R. Speck, E. Storm, J. E. Swain, L. W. Coleman, C. D. Hendricks, H. N. Kornblum, F. D. Seward, V. W. Slivinsky, Y. L. Pan, G. B. Zimmerman, J. H. Nuckolls, "Implosion Experiments with an Asymmetrically Irradiated Laser Fusion Target." Plasma Phys. 18, 675 (1976).

7. A. R. Thiessen and J. T. Larsen, "Computer Simlation of Recent Laser Driven Implosions of Glass Microshells," Bull. Am. Phys. Soc. 21, 1190 (1976).

8. R. A. Haas, W. C. Mead, W. L. Kruer, D. W. Phillion, H. N. Kornblum, J. D. Lindl, D. MacQuig, V. C. Rupert, K. G. Tirsell, "Irradiation of Parylene Disks with a 1.06μm Laser," Phys. Fluids 20, 322 (1977).

9. D. W. Forslund, J. M. Kindel, K. Lee, "Theory of Hot Electron Spectra at High Laser Intensity," to be published in Phys. Rev. Lett. (1977).

10. V. M. Cottles and D. V. Giovanielli, "The Absorption of 1-ns CO_2 Laser Pulses by Plane Targets," to be presented at the 7th Annual Symposium on the Anomalous Absorption of Intense High-Frequency Waves, Ann Arbor, Michigan, May 1977.

11. G. B. Zimmerman and W. L. Kruer, "Numerical Simulation of Laser-Initiated Fusion," Comments in Plasma Physics and Controlled Fusion 2, 51 (1975).